

Observational Properties of β Cephei Stars: 88 new samples discovered Based on TESS and Gaia Data

XIANG-DONG SHI,^{1,2} SHENG-BANG QIAN,³ LI-YING ZHU,^{1,2} LIN-JIA LI,^{1,2} ER-GANG ZHAO,^{1,2} DAVID MKRTICHIAN,⁴
FARKHODJON KHAMRAKULOV,⁵ AND WEN-XU LIN^{1,2}

¹Yunnan Observatories, Chinese Academy of Sciences(CAS), P.O. Box 110, Kunming 650216, People's Republic of China

²University of Chinese Academy of Sciences, No.1 Yanqihu East Rd, Huairou District, Beijing 101408, People's Republic of China

³Department of Astronomy, Key Laboratory of Astroparticle Physics of Yunnan Province, Yunnan University, Kunming 650091, People's Republic of China

⁴National Astronomical Research Institute of Thailand, 260 Moo 4, T. Donkaew, A. Maerim 50180, Chiangmai, Thailand

⁵Samarkand State University named after Sharof Rashidov, Engineering Physics Institute, Department of Nuclear Physics and Astronomy, University blv. 15, 140104 Samarkand, Uzbekistan

ABSTRACT

We present a systematic investigation of β Cephei (BCEP) stars by integrating photometric data from the Transiting Exoplanet Survey Satellite (TESS) with astrometric parameters from Gaia Data Release 3. Utilizing TESS's short-cadence (SC) and full-frame image (FFI) photometry, along with Gaia parallaxes and temperatures derived from the Extended Stellar Parametrizer for Hot Stars (ESP-HS) pipeline, we identify 88 new BCEP stars and candidates—85 from SC data and 3 from SPOC-processed FFI observations. These targets exhibit visual magnitudes ranging from 8.0 to 12.0 mag, parallaxes between 0.11 and 1.74 mas, effective temperatures of 18,000 to 30,000 K, and luminosities from 1,500–38,000 L_{\odot} , consistent with previously cataloged BCEP populations, thereby demonstrating the robustness of our classification criteria. Key findings include: (1) a significant detection disparity between SC and FFI datasets, with 30% of SC targets exceeding 18,000 K compared to only 0.7% in FFI, reflecting observational biases toward high-luminosity, hotter stars in SC data; (2) four samples near the red edge of the theoretical instability strip, exhibiting sparse pulsation modes that are important samples for testing pulsation models under low-mass, low-temperature conditions; and (3) spatial clustering within the Galactic disk ($|b| < 20^{\circ}$), with two high-latitude outliers likely representing runaway stars ejected from disk environments. Our analysis underscores the critical role of space-based photometry in detecting low-amplitude pulsators and the transformative potential of multi-survey integration in the era of time-domain astronomy. These results provide new samples to constrain stellar pulsation theories of massive stars and to study Galactic dynamics.

Keywords: Massive stars (732) — Pulsating variable stars (1307)

1. INTRODUCTION

Massive stars, which serve as progenitors of compact objects such as neutron stars and black holes, are the source of extreme astrophysical events, including supernova explosions, mergers of compact binaries, and gravitational wave radiation (Sadowski et al. 2008; Yoon et al. 2010; Han et al. 2020; Langer et al. 2020). Simultaneously, these stars play a crucial role in the chemical enrichment of galaxies through supernova explosions and stellar wind mass loss, which directly influence the distribution of metal abundance in the interstellar medium (Vink et al. 2001). In the field of stellar evolution, massive pulsating variables—with their unique oscillatory properties—serve as essential probes for asteroseismology, helping to unravel stellar internal structures and evolutionary laws (e.g., Aerts et al. (2003); Mazumdar et al. (2006); Aerts et al. (2006); Handler et al. (2006); Dziembowski & Pamyatnykh (2008); Briquet et al. (2012)). Currently, only two classes of massive pulsators are recognized on upper main sequence stars: Slowly Pulsating B-type (SPB) stars and β Cephei (BCEP) stars. Among these, BCEP stars are considered a "key laboratory" for studying massive star evolution due to their distinctive physical properties.

Compared to SPB stars, BCEP stars occupy a higher mass range. Their lower mass limit is generally established at $7 M_{\odot}$, while the upper limit remains uncertain, potentially extending beyond $20 M_{\odot}$. This corresponds to late O-type to early B-type spectral classifications (Miglio et al. 2007). BCEP stars represent the most massive group of standing-wave pulsators discovered on the main sequence. Their pulsations are driven by the κ -mechanism in the ionization zone of iron-group elements (Moskalik & Dziembowski 1992; Dziembowski & Pamiatnykh 1993), predominantly exhibiting low-order pressure modes (p-modes) and often including gravity modes (g-modes). The most prominent pulsation periods range from 2 to 7 hours (Stankov & Handler 2005; Aerts et al. 2010).

Since p-modes and g-modes traverse the radiative envelope and convective core of a star, respectively, their oscillation spectra encode multidimensional structural information from the core to the envelope (e.g., Kurtz (2006)). This provides asteroseismology with unique, multi-layered diagnostic capabilities, offering invaluable advantages in constraining parameters such as the size of convective cores in massive stars, convective core overshooting, internal rotation profiles, and chemical stratification (e.g., Pedersen et al. (2021); Burssens et al. (2023)).

Despite their astrophysical significance, only 400 to 500 Galactic BCEP stars have been cataloged (e.g., Stankov & Handler (2005), Pigulski & Pojmański (2008), Burssens et al. (2019), Labadie-Bartz et al. (2020), Balona & Ozuyar (2020)). The advent of large-scale astronomical surveys, including the Transiting Exoplanet Survey Satellite (TESS; Ricker et al. (2015)) and the Gaia mission (Gaia Collaboration et al. 2016, 2018, 2021), has revolutionized the systematic investigation of variable stars through extensive, high-precision datasets (e.g., Shi et al. (2023a,b, 2024), hereafter referred to as Papers I, II, and III). For BCEP stars—characterized by low-amplitude pulsations—the continuous and high-precision time-series photometry from space-based observatories provides unparalleled capabilities for their detection and characterization (e.g., Papers I and III, Balona & Ozuyar (2020); Eze & Handler (2024)). By leveraging data from TESS and Gaia, this study presents new discoveries of BCEP stars and systematically analyzes their observational properties.

2. DATA AND METHOD

2.1. TESS and Gaia Data

TESS, a NASA mission led by MIT, conducts an all-sky survey to detect transiting exoplanets. TESS employs four identical cameras, each with a $24^{\circ} \times 24^{\circ}$ field of view, which collectively form $24^{\circ} \times 96^{\circ}$ sky strips designated as “sectors”. For each sector, TESS acquires full-frame images (FFI) at a cadence of 30 minutes or shorter, while simultaneously collecting short-cadence (SC) data of 2-minute or shorter for approximately 20,000 pre-selected targets. The FFI data is selectively processed for brighter stars, and all short-cadence observations are systematically processed through the Science Processing Operations Center (SPOC). The stellar catalog includes nearly one million targets with short-cadence photometry, while the SPOC-processed FFI (FFI-SPOC) data contains more than five times this quantity. Beyond its primary objective of exoplanet detection, TESS’s high-precision, large-volume photometric datasets have been proven invaluable for identifying and characterizing bright variable stars (e.g., Balona & Ozuyar (2020); Shi et al. (2022)).

An analysis of BCEP star characteristics reveals that these objects rarely exhibit pulsation frequencies exceeding $20 d^{-1}$ (Papers I and III). This observational property makes both the FFI data and the SC data from TESS suitable for their study, since even the FFI data at the maximum 30-minute cadence (corresponding to a Nyquist frequency of $24 d^{-1}$) is sufficient to capture the highest expected pulsation frequencies.

This study analyzed light curve data obtained from the Mikulski Archive for Space Telescopes (MAST), comprising TESS-SC data for Sectors 1–69 and FFI-SPOC data for Sectors 1–55. Due to the low likelihood of detecting BCEP stars in the FFI-SPOC data, the analysis of Sectors 56–69 is not included in the current work and is scheduled for the next phase. We specifically utilized the Pre-search Data Conditioned Simple Aperture Photometry (PDCSAP) flux measurements (Jenkins et al. 2010) due to their superior corrections for systematic instrumental variations and their effectiveness in mitigating scattered light contamination compared to standard aperture photometry products. Following the methodology outlined in Shi et al. (2021a,b), our pipeline processes the data through flux-to-magnitude conversion and subsequent mean magnitude subtraction, effectively generating light curves that are equivalent to differential photometry.

The Gaia satellite, launched by the European Space Agency (ESA) on December 19, 2013, has collected exceptionally high-precision astrometric data for nearly two billion stars (Gaia Collaboration et al. 2016, 2018, 2021). Its parallax measurements serve as a cornerstone for determining stellar luminosities, providing an independent methodology for investigating variable stars (e.g., Murphy et al. (2019)) and validating the reliability of astrophysical studies (e.g.,

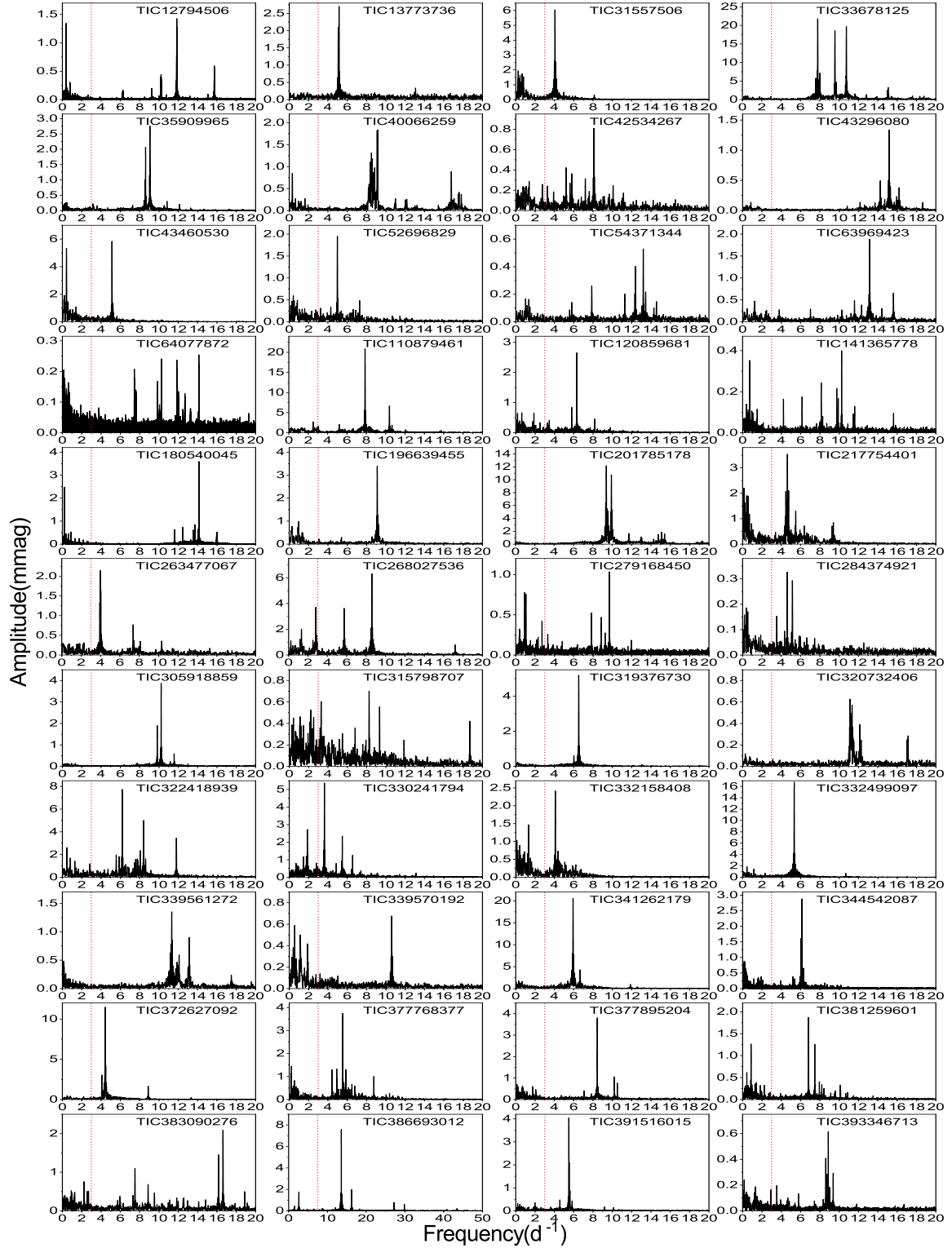


Figure 1. Fourier spectra of new BCEP stars and candidates. The red dotted lines are the rough boundary ($3 d^{-1}$) for low-frequency and high-frequency.

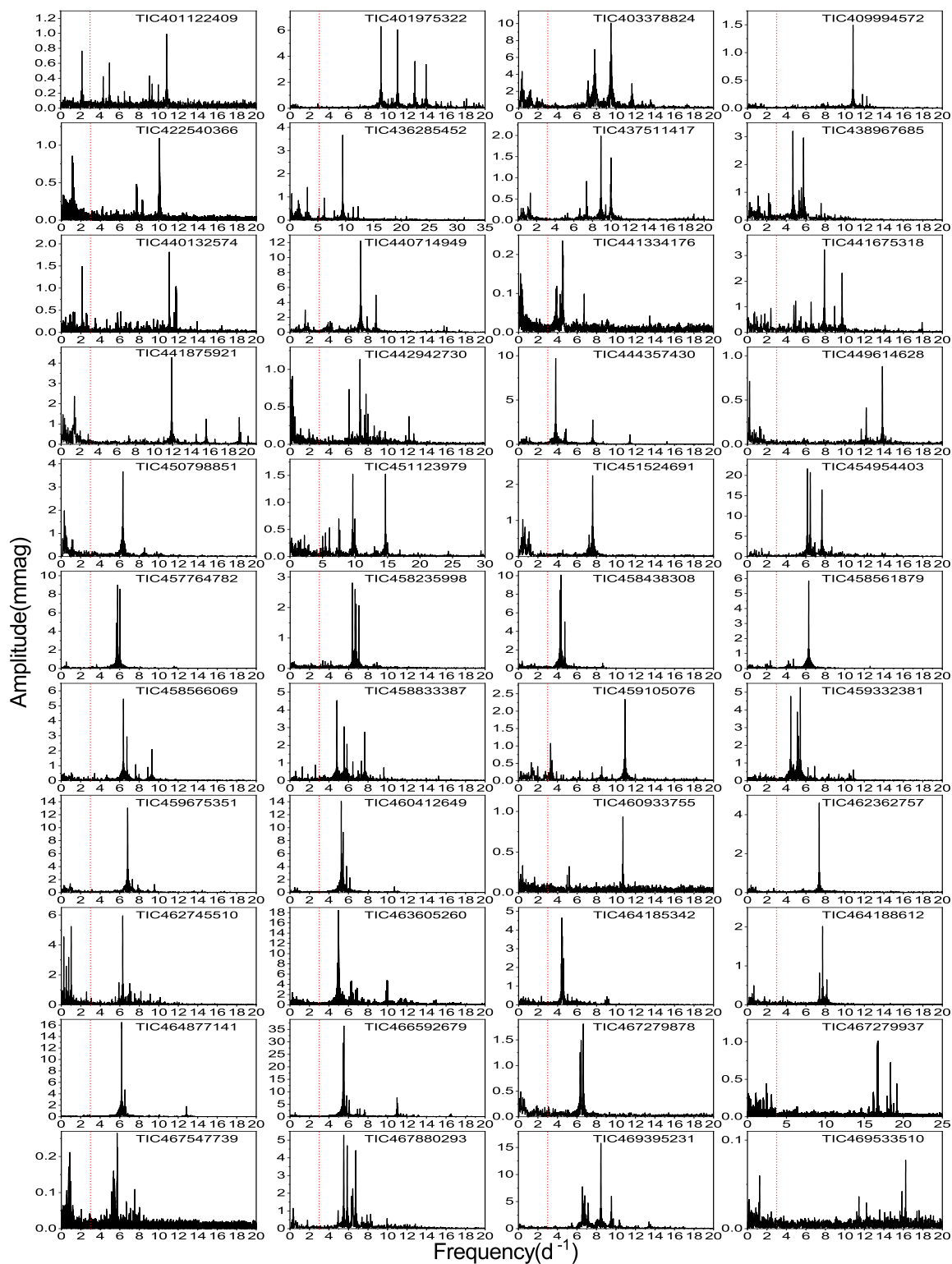


Figure 1. (Continued.)

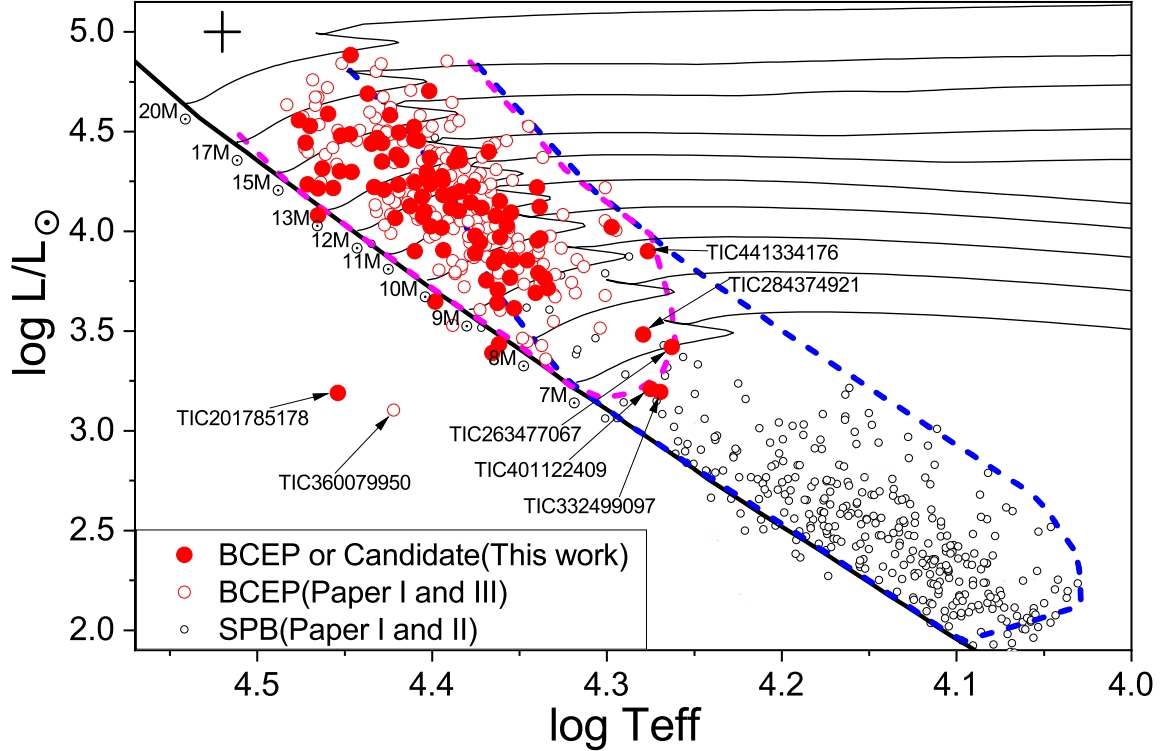


Figure 2. The Hertzsprung–Russell (H–R) diagram of BCEP stars. In this diagram, confirmed BCEP stars and candidates from this work are marked as filled red circles. For comparative analysis, previously published BCEP and SPB stars from Paper I–III are also plotted as open red circles and black circles, respectively. Theoretical stellar evolution frameworks are shown, Black solid curves: Zero-age main sequence (ZAMS) and evolutionary tracks for masses 7–20 M_{\odot} at solar metallicity ($Z = 0.02$); Blue/magenta dashed curves: the theoretical instability strips for SPB/BCEP stars at $Z = 0.02$, modeling low-degree pulsation modes $l \leq 3$ (Miglio et al. 2007); Black cross: a standard error box.

Shi et al. (2021c)). The stellar atmospheric parameters in Gaia Data Release 3 (DR3) are derived through multiple methodologies that utilize data from the Blue and Red Photometer (BP/RP) low-resolution spectra and Radial Velocity Spectrometer (RVS) observations. Given the high temperatures of our targets, we will employ the stellar atmospheric parameters derived from the Extended Stellar Parametrizer for Hot Stars (ESP-HS) pipeline in this study.

2.2. Classification

Building on our previous TESS-based investigations of BCEP stars (Papers I and III), this study identifies 85 new BCEP stars or candidates through the analysis of TESS-SC data, with 32 originating from Sectors 1–55 and 53 from Sectors 56–69. Additionally, expanding the survey to include TESS FFI-SPOC data of Sectors 1–55 reveals only three new candidates (TIC201785178, TIC263477067, and TIC401122409). Among these 88 sources, TIC386693012 and TIC459105076, previously classified as candidate pulsators by Labadie-Bartz et al. (2020), are now unambiguously confirmed as BCEP stars for the first time. The fundamental parameters and pulsation properties of these BCEP stars or candidates are summarized in Table 1.

The detailed identification criteria for BCEP stars are outlined in Papers I and III. These criteria primarily include the Fourier spectral features derived from light curve analysis, as well as the positional distributions in Hertzsprung–Russell (H–R) diagrams, the temperature–period (T–P) diagrams, and the luminosity–period (L–P) diagrams. Except for six objects, which are temporarily classified as candidates for BCEP stars (denoted as “BCEP?”) due to their partial fulfillment of the identification criteria, all other targets are ultimately identified as BCEP stars and marked as “BCEP” in column (10) of Table 1.

Given the angular resolution of TESS (21'' per pixel), we conducted a systematic assessment of contamination for all targets by examining potential flux contributions from neighboring stars within the photometric aperture. Utilizing image data from SIMBAD and high-precision astrometry from Gaia, we cross-matched all sources within a 1-arcminute

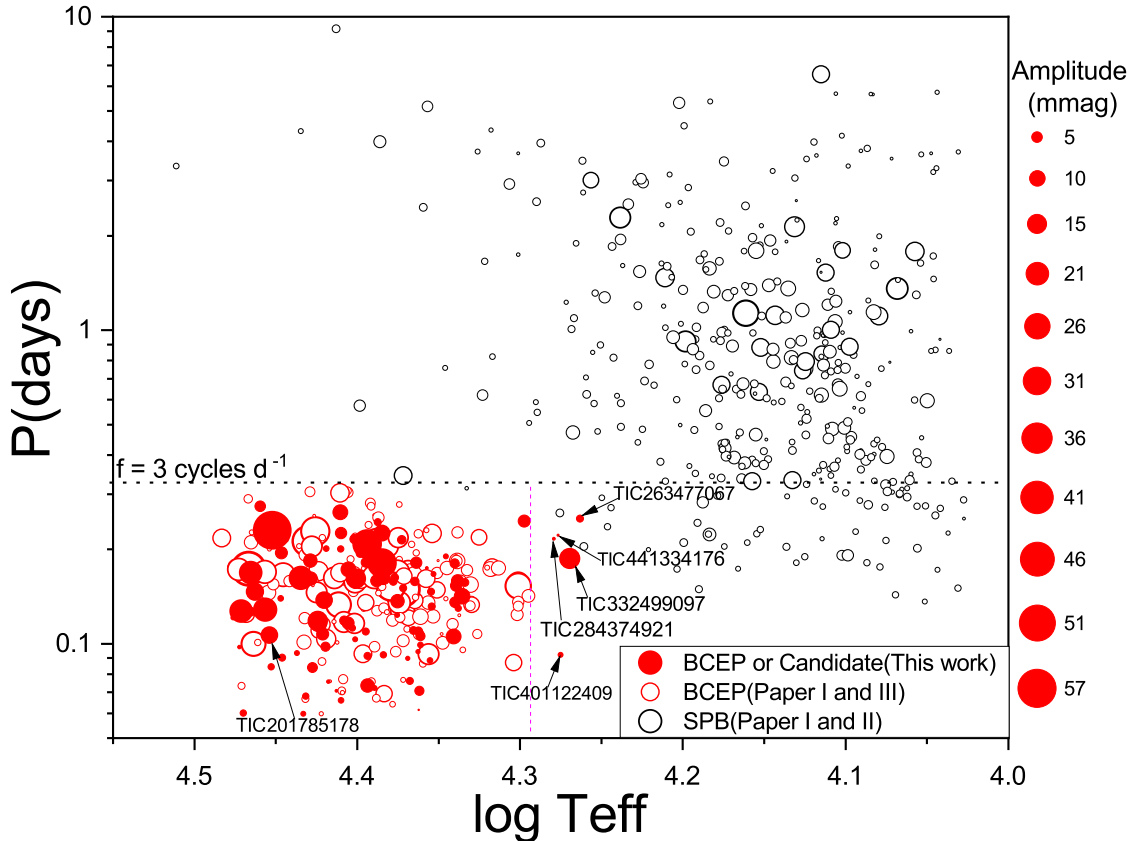


Figure 3. The effective temperature and the dominant pulsating period relation diagram of these BCEP stars and candidates. Similar symbols to those in Figure 2 are used, but the size of the circles denotes their pulsation amplitude at the dominant frequency.

diameter centered on each target, and then .pdfd the capital letter "C" in column 10 of Table 1 to indicate the targets that may be contaminated.

We also employed the TESS-Localize software (Higgins & Bell 2023) to determine the spatial origin of the light variations. This tool utilizes observed frequencies as input parameters to compute optimal signal source locations within the specified Target Pixel File (TPF). To evaluate the fitting quality, the software provides two statistical metrics: (1) relative likelihood, which quantifies the probability distribution of potential source stars matching the fitted location; and (2) p-values, which test the hypothesis that each star's position is consistent with the derived signal origin. In this work, a signal is considered to originate from our target source if it has the highest relative likelihood (>60%) and the highest p-value (>0.1) among all sources within its TPF. As a result, we found that the prominent signals for nearly all targets originated from their intended stars, with two exceptions. First, we excluded one target (TIC 460689513, it should be a B-type star contaminated by a Delta Scuti variable) originally classified as a BCEP star under other criteria. Second, we confirmed that the apparent variability detected in TIC 464732837 is due to contamination from the nearby pulsating star TIC 464732844.

3. RESULTS

3.1. Stellar Parameters

Table 1 presents the astrophysical parameters of 88 BCEP stars and candidates analyzed in this study. Column (2) lists the Gaia DR3 parallaxes π with typical uncertainties of 0.05 mas. The visual magnitudes m_V in Column (3) were systematically derived from the TESS Input Catalog (TIC; Stassun et al. (2018)) or from SIMBAD (Wenger et al. 2000).

The bolometric correction BC in Column (4) was derived from the hybrid local thermodynamic equilibrium/non-local thermodynamic equilibrium (LTE/NLTE) grid of Pedersen et al. (2020), which provide temperature-dependent

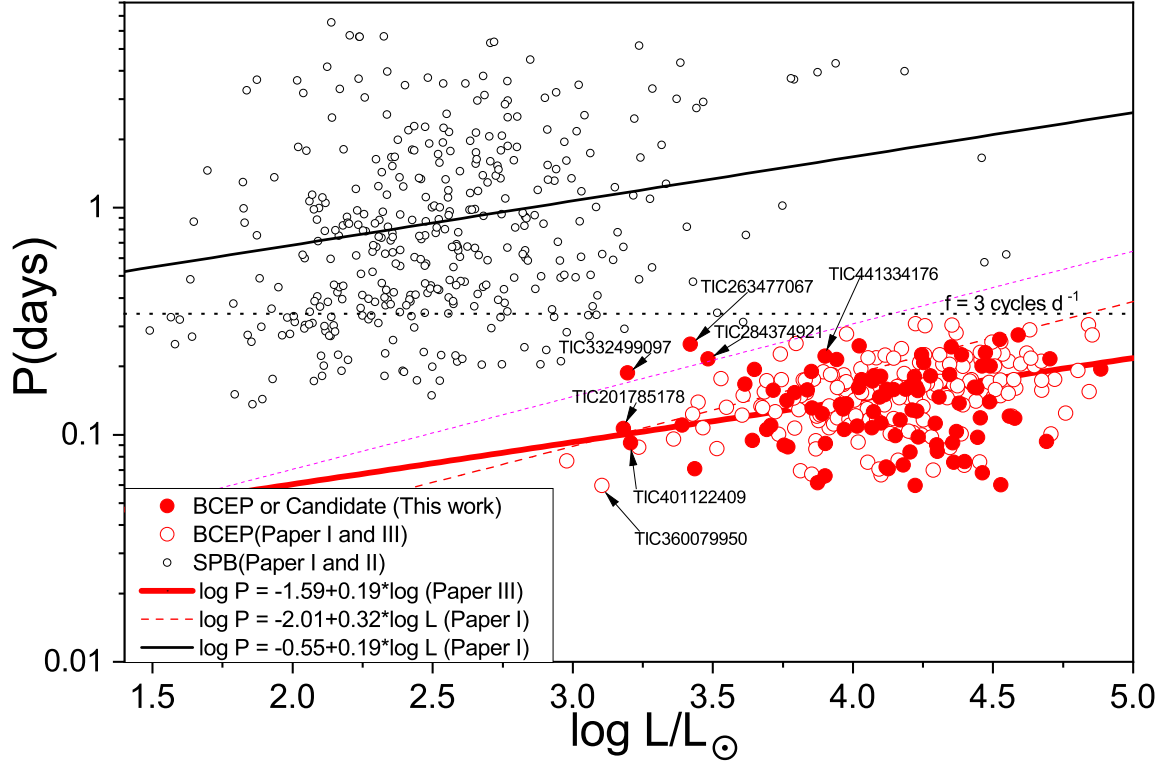


Figure 4. The luminosity and the dominant pulsating period relation diagram of these BCEP stars and candidates. Symbols are similar to those in Figure 4. The red dashed line and the black solid line represent the relationship derived by Paper I for BCEP and SPB stars, respectively. The red solid line represents the new relation derived in Paper III.

calibrations for the Johnson V passband. As demonstrated in our previous work (Papers I and II), the Gaia ESP-HS spectroscopic catalog offers reliable temperature determinations for hot stars, with systematic uncertainties typically below 10% across the parameter space of BCEP stars. Consequently, both the effective temperatures T_{eff} and interstellar extinction values A_V listed in Columns (6) and (5) of Table 1, respectively, were adopted from the Gaia ESP-HS catalog, applying significant digit selection to ensure their physical relevance.

The stellar luminosities in Column (7) were calculated using the following formulas:

$$\log(L/L_{\odot}) = 0.4 \times (4.74 - M_V - BC) \quad (1)$$

where the absolute magnitude M_V is determined by:

$$M_V = m_V - 5 \times \log(1000/\pi) + 5 - A_V, \quad (2)$$

Error propagation analysis, which considers typical parameter uncertainties ($\sigma_{\pi} = 0.05$ mas, $\sigma_{A_V} = 0.10$ mag, $\sigma_{BC} = 0.02$ mag, $\sigma_{m_V} = 0.01$ mag), yields a mean luminosity uncertainty of $\sigma_{\log L} \approx 0.1$ dex. This result is consistent with the precision levels reported in recent studies of massive pulsators (Balona & Ozuyar 2020).

The 88 targets exhibit the visual magnitudes spanning 8.0–12.0 mag, the parallaxes between 0.11 and 1.74 mas, the effective temperatures of 18,000–30,000 K, and the bolometric luminosities ranging from 1,500 to 38,000 L_{\odot} . These parameter distributions are consistent with those reported in Paper III.

3.2. Pulsation Properties

The Fourier spectra of the light curves for these BCEP stars and candidates were processed using the Period04 software (Lenz & Breger 2005), with the resulting frequency analyses presented in Figure 1. The signal-to-noise ratio (S/N), defined as the ratio of the pulsation amplitude to the local noise floor (calculated within a $1 d^{-1}$ frequency bin), serves as the primary criterion for assessing the statistical significance of detected frequencies. Following the methodology of Baran & Koen (2021), we adopt a detection threshold of $S/N \geq 5.4$ for SC data and $S/N \geq 5.0$ for FFI data.

Adopting the period range of p-mode ($P < 0.3$ days; Aerts et al. 2010; Stankov & Handler 2005), we empirically define $3 d^{-1}$ as an operational threshold separating low-frequency and high-frequency domains in the Fourier spectrum. As discussed in Paper III, frequencies above this threshold are unlikely to originate from binarity or rotational modulation, as their corresponding equatorial rotation velocities will be greater than $600 \text{ km} \cdot \text{s}^{-1}$.

Columns (8)–(9) of Table 1 present the pulsation periods (P) and amplitudes (A) corresponding to the dominant frequencies, with uncertainties in the last decimal place provided in parentheses following the methodology of Montgomery & Odonoghue (1999). The data reveal pulsational characteristics spanning $P=0.06\text{--}0.27$ days and $A = 0.1\text{--}56$ mmag in the TESS band, consistent with typical BCEP variables reported in Paper III.

Figure 2–4 show the positional distributions of these BCEP stars and candidates in H–R diagram, T–P diagram, and L–P diagram. In the H–R diagram, we present the theoretical Zero Age Main Sequence (ZAMS) and the evolutionary tracks of stars with different masses (black solid lines) created using the stellar evolution code Modules for Experiments in Stellar Astrophysics (Paxton et al. 2011, 2013, 2015, 2018, 2019), as well as the theoretical unstable regions of SPB and BCEP stars (blue and magenta dashed lines) given by Miglio et al. (2007).

The H–R diagram (Figure 2) reveals that, with the exception of TIC201785178, all targets occupy the main-sequence region coinciding with the theoretical instability strip of BCEP stars. TIC201785178 displays a characteristic pulsational spectrum of BCEP stars, with a Gaia parallax of 1.59 mas that is the second-highest value among the samples in both this work and Paper III. Notably, SIMBAD classifies this object as a double or multiple star system. It is likely a BCEP star, and its lower luminosity may be caused by unreliable parallax measurements due to the orbital motion of binary or multiple system, but it may also be a subdwarf star in a binary system. The situation of TIC201785178 is very similar to TIC360079950 discussed in Paper III.

The T–P diagram (Figure 3) demonstrates that all targets except five objects (TIC263477067, TIC441334176, TIC332499097, TIC284374921, and TIC401122409) are co-located with the BCEP stars in the same parameter space as those reported in Paper III. TIC263477067, TIC284374921, TIC332499097, and TIC401122409 are located in the low-mass (red) end of the theoretical pulsational instability strip, which is usually sparsely populated in observational surveys (e.g., Stankov & Handler (2005)). Furthermore, our analysis reveals that their light curves yield a limited number (< 10) of significant pulsation frequencies, likely attributable to restricted mode excitation near the theoretical instability strip boundary. Therefore, although their distribution in the H–R, T–P, or L–P diagrams is different from other BCEP stars, they are still suspected to be BCEP stars, and marked as candidates. They will be excellent samples for studying the red end of theoretical instability strip. Unlike the other four targets, TIC 441334176 exhibits more than ten significant pulsation frequencies, and its location on the H–R diagram preliminarily indicates that it is an $8\text{--}9 M_{\odot}$ star near the main-sequence turnoff. In comparison, the other four targets are probable main-sequence stars of below $7.5 M_{\odot}$ located nearer to the red edge.

The L–P diagram (Figure 4) reveals that most these new objects are consistent with the empirical relationship established in Paper III. However, TIC263477067, TIC332499097, and TIC284374921 display significant deviations from this relationship.

3.3. The Spatial Distribution of β Cephei Stars

The galactic spatial distribution of BCEP stars from this study (solid circles), as well as from Papers I and III (open circles), is illustrated in Figure 5. The sizes of the symbols correspond to the Gaia parallax π , with larger symbols indicating shorter distances. These samples encompasses heliocentric distances ranging from 0.6 to 8 kpc, with a predominant concentration in the Galactic disk (Galactic latitude $|b| < 20^{\circ}$).

Notable outliers, TIC352229000 and TIC65516748, located at high Galactic latitudes, likely formed in the Galactic halo or represent runaway stars ejected from the disk (Ramspeck et al. 2001). Gaia DR3 astrometry reveals exceptionally high proper motions for both targets: TIC352229000 exhibits $(\mu_{\alpha}, \mu_{\delta}) = (16.48, -18.72) \text{ mas yr}^{-1}$, while TIC65516748 displays $(\mu_{\alpha}, \mu_{\delta}) = (-6.78, -7.80) \text{ mas yr}^{-1}$. These values significantly exceed the median proper motion of Galactic disk stars ($\sim 1\text{--}5 \text{ mas yr}^{-1}$) (Gaia Collaboration et al. 2021), translating to transverse velocities of $\sim 317 \text{ km s}^{-1}$ and 85 km s^{-1} , respectively. This is a relatively large value, we classify both objects as runaway stars, likely ejected through either dynamical interactions in dense stellar environments or binary supernova recoil mechanisms.

3.4. Detection Constraints of TESS

We compared the parallax, visual magnitude, and temperature distribution of high-temperature stars ($T > 10,000 \text{ K}$ provided by GAIA ESP-HS) with TESS-SC and FFI-SPOC data from Sector 1 to 55. As illustrated in Figure 6, the

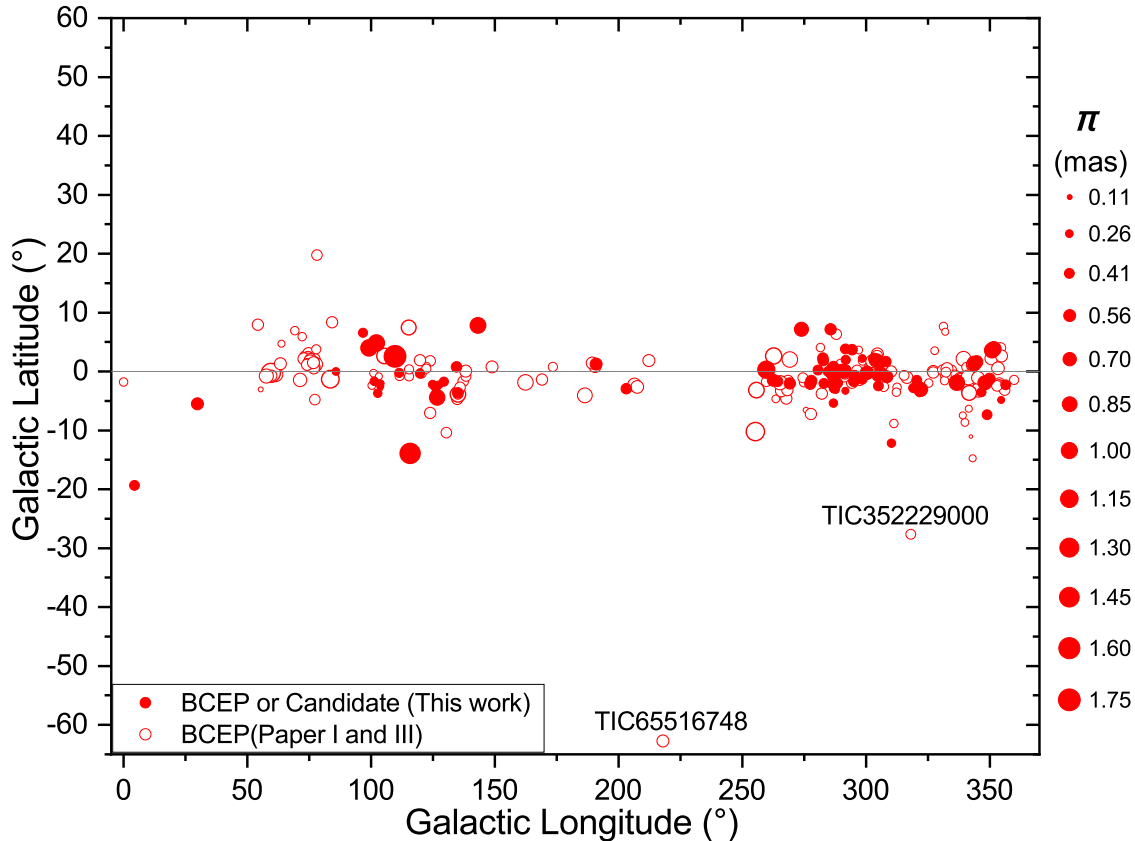


Figure 5. The Distribution of BCEP stars according to Galactic longitude and latitude. Similar symbols to these BCEP stars in Figure 2 are used, but the size of the circles denotes their parallaxes π .

peak visual magnitudes for TESS-SC and FFI-SPOC targets are centered at 8 mag and 11 mag, respectively, with corresponding peak parallax values of 0.5 mas and 1.0 mas. This correlation between visual magnitude and parallax suggests that FFI-SPOC predominantly captures these lower luminosity stars compared to TESS-SC.

Assuming these stars are main-sequence stars, the lower luminosity of FFI-SPOC targets further implies systematically cooler temperatures relative to their TESS-SC counterparts, a trend quantitatively supported by the temperature histograms in the right panels of Figure 6. Among stars with TESS-SC data, approximately 30% exhibit temperatures exceeding 18,000 K, whereas only 0.7% of stars with FFI-SPOC data have temperatures exceeding 18000K. Therefore, only 3 candidates were identified within the FFI-SPOC data in this work. Notably, our companion study (Paper II), which analyzed hot star populations cataloged by LAMOST spectroscopic surveys, did not detect any confirmed BCEP stars or candidates.

The angular resolution of TESS (21'' per pixel) imposes significant challenges in resolving targets within densely populated regions of the Galactic disk, particularly toward the Galactic center. In such crowded fields, distant BCEP stars (located at heliocentric distances > 5 kpc) are prone to blending with neighboring stars within the photometric aperture. This contamination artificially inflates flux measurements, suppresses detectable pulsation amplitudes, and complicates the extraction of clean light curves. For example, in the Galactic plane near the bulge ($|\ell| < 30^\circ$, $|b| < 10^\circ$), the high stellar density (exceeding 10^3 stars deg^{-2} ; (Gaia Collaboration et al. 2021)) exacerbates these issues, leading to potential misclassifications or missed detections of genuine BCEP stars. This effect partially explains the scarcity of BCEP candidates in FFI-SPOC data and the absence of BCEP stars in Paper II’s LAMOST sample.

However, these conclusions are primarily a result of observational selection effects, and they may change with evolving observing strategies and the pre-selected targets of TESS. For instance, the strategy in TESS Sectors 56–69 targeted numerous new massive stars, which is the direct reason we were able to identify 53 additional targets from these data.

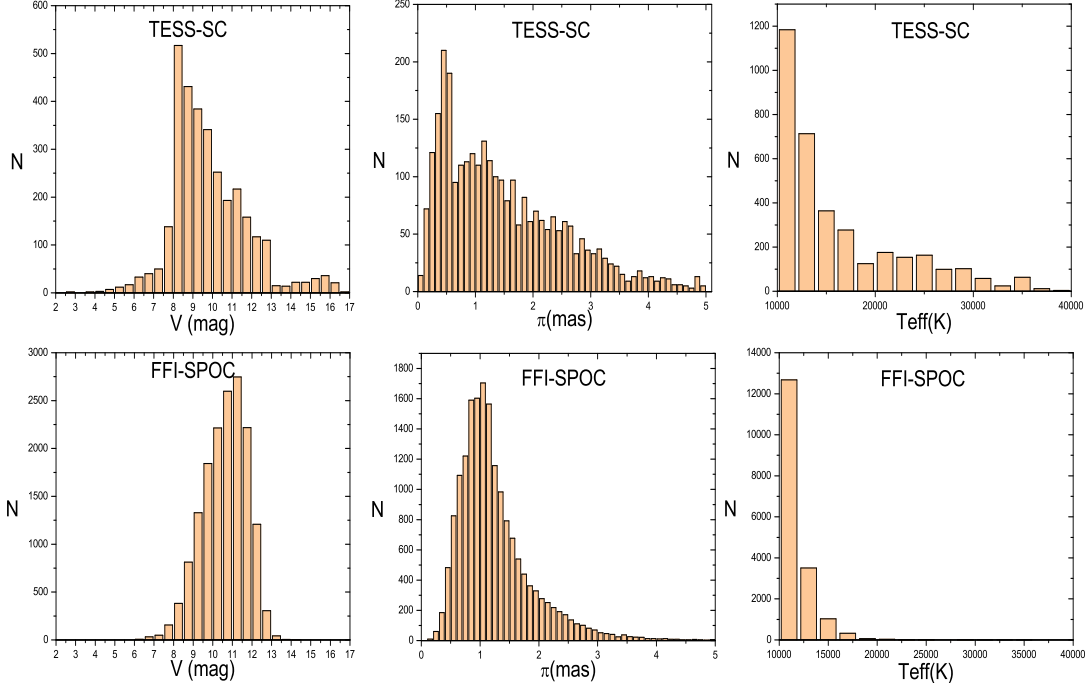


Figure 6. Distribution of the parallax, visual magnitude, and temperature for high-temperature stars ($T > 10,000K$) with TESS-SC and FFI-SPOC data.

4. DISCUSSION AND CONCLUSION

Through the integration of TESS photometric data with Gaia spectral and astrometric observations, we have identified 82 new confirmed BCEP stars and 6 candidates from TESS-SC and FFI-SPOC data. These discoveries indicate the parameter space of BCEP stars to visual magnitudes of 8.0–12.0 mag, parallaxes of 0.11–1.74 mas, effective temperatures of 18,000–30,000 K, and luminosities spanning 1,500–38,000 L_{\odot} , consistent with the characteristics of BCEP stars outlined in Paper III.

In the H-R diagram, the anomalous object TIC201785178 attributed to potential binarity or multiplicity, mirrors the case of TIC360079950 in Paper III. Such systems require follow-up radial velocity monitoring to disentangle orbital and pulsational signals, as unresolved companions may distort parallax-based luminosity estimates. Similarly, TIC263477067, TIC284374921, TIC332499097, and TIC401122409 are located near the red boundary of the instability strip in the H-R diagram, and their inhibited pulsation mode excitation suggests that they are excellent samples for testing the red boundary of the theoretical pulsation model for BCEP stars.

The spatial distribution of BCEP stars, as shown in Figure 5, demonstrates a significant concentration within the Galactic disk ($|b| < 20^{\circ}$). This pattern aligns with their massive, short-lived characteristics and their origins in star-forming regions. The outliers TIC352229000 and TIC65516748, located at high Galactic latitudes, likely represent runaway stars that have been ejected from the disk (Ramspeck et al. 2001) or remnants of disrupted dwarf galaxies. These stars provide valuable insights into the dynamical processes occurring in the halo.

The comparative analysis of the TESS-SC and FFI-SPOC datasets reveals significant observational biases in the detection of BCEP stars. TESS-SC targets predominantly capture brighter, higher-mass stars, but FFI-SPOC data are skewed toward fainter, lower-luminosity objects. This luminosity disparity corresponds to a systematic temperature difference—only 0.7% of FFI-SPOC targets exceed 18,000 K, compared to 30% in the TESS-SC data. Consequently, FFI-SPOC observations yielded only three BCEP candidates, highlighting the challenges of identifying high-temperature pulsators at fainter magnitudes. The scarcity of BCEP stars in the FFI-SPOC data may also reflect limitations in photometric precision for low-amplitude pulsations or contamination from blended sources due to TESS’s coarse angular resolution of $21''$ per pixel. Future missions with higher spatial resolution and extended time-series coverage

will be essential for disentangling blended sources and exploring the distant, high-density regions of the Galactic disk where massive pulsators may remain concealed.

These results underscore the significance of high-precision, uninterrupted space photometry from TESS in identifying low-amplitude bright pulsators, as well as the value of Gaia's astrometric precision in validating astrophysical parameters. As TESS data continue to be updated and only a subset has been analyzed thus far, the present study should not be regarded as complete. Future work will focus on broadening the search scope and performing a systematic reclassification of BCEP stars identified by other teams, with the overarching aim of establishing a consistent characterization framework for the entire BCEP class. In subsequent studies, priority should also be given to the following: high-resolution spectroscopy to confirm binarity in outliers (e.g., TIC 201785178) and to measure rotational velocities; and extended pulsation mode analysis for samples near the boundaries of the instability strip.

Table 1. The Catalog of BCEP stars and candidates newly identified from TESS and Gaia data.

TESS ID	π (<i>mas</i>)	V (<i>Mag</i>)	BC (<i>Mag</i>)	A_V (<i>Mag</i>)	T_{eff} (<i>K</i>)	$\log(L/L_{\odot})$	Period (<i>days</i>)	Amplitude (<i>mmag</i>)	Comments	Flag
12794506	1.74	9.90	-2.79	4.33	28400(400)	4.30	0.084451671(1)	1.42 (1)	BCEP	
13773736	0.45	13.45	-2.48	3.63	25000(500)	3.65	0.194130664(1)	2.65 (4)	BCEP(C)	
31557506	0.38	8.89	-1.92	0.16	19800(100)	4.02	0.246114383(3)	6.05 (1)	BCEP	
33678125	0.38	9.97	-2.81	0.85	28600(500)	4.21	0.128415381(1)	21.82(1)	BCEP	
35909965	0.74	9.45	-2.30	0.23	23200(400)	3.39	0.110331215(1)	2.85 (1)	BCEP	
40066259	0.88	9.36	-2.46	1.92	24800(500)	4.01	0.109273377(1)	1.84 (1)	BCEP	
42534267	0.94	8.35	-2.36	0.84	23700(300)	3.89	0.123628955(1)	0.81 (1)	BCEP(C)	
43296080	0.85	8.73	-2.55	0.85	25700(500)	3.90	0.065957204(1)	1.32 (1)	BCEP	
43460530	0.41	10.43	-2.76	3.20	28000(500)	4.88	0.194801805(1)	5.84 (1)	BCEP(C)	
52696829	0.31	10.80	-2.55	2.12	25700(500)	4.46	0.200818875(3)	1.95 (2)	BCEP(C)	
54371344	0.36	10.70	-2.59	2.06	26200(600)	4.36	0.075740829(1)	0.49 (1)	BCEP	
63969423	0.16	11.87	-2.31	1.83	23300(400)	4.40	0.076134460(1)	1.82 (1)	BCEP	
64077872	0.22	11.63	-2.56	1.36	25900(500)	4.13	0.070792469(1)	0.25 (1)	BCEP(C)	
110879461	0.38	11.69	-2.90	2.54	29600(600)	4.23	0.126993380(1)	20.88(2)	BCEP	
120859681	0.51	8.88	-2.37	0.68	23900(200)	4.14	0.158119787(1)	2.78 (1)	BCEP	
141365778	0.55	10.62	-2.90	2.78	29700(400)	4.44	0.097590761(1)	0.39 (1)	BCEP	
180540045	1.13	8.98	-2.28	0.81	23000(400)	3.43	0.070782259(1)	3.58 (1)	BCEP	
196639455	0.78	9.48	-2.28	1.19	23000(500)	3.71	0.109794376(1)	3.39 (1)	BCEP(C)	
201785178	1.59	10.96	-2.80	2.37	28400(2100)	3.18	0.106536298(1)	12.14(2)	BCEP?(C)	
217754401	0.33	10.01	-2.50	2.12	25200(500)	4.70	0.215771750(3)	3.53 (1)	BCEP(C)	
263477067	0.41	11.10	-1.72	1.27	18300(400)	3.42	0.250900812(1)	2.18 (2)	BCEP?	
268027536	0.45	9.39	-2.53	0.80	25400(300)	4.17	0.116430153(1)	6.32 (1)	BCEP(C)	
279168450	0.23	11.52	-2.50	2.03	25200(500)	4.37	0.103186418(1)	1.00 (2)	BCEP(C)	
284374921	0.75	9.51	-1.82	1.03	19000(100)	3.48	0.216285812(2)	0.33 (1)	BCEP?(C)	
305918859	0.41	9.82	-2.60	1.10	26300(500)	4.23	0.097811596(1)	3.85 (1)	BCEP(C)	
315798707	0.45	8.92	-2.92	0.94	29900(300)	4.56	0.120953136(1)	0.70 (1)	BCEP	
319376730	0.58	9.40	-2.15	0.79	21800(300)	3.79	0.153347065(1)	5.19 (1)	BCEP(C)	
320732406	0.43	10.64	-2.32	1.15	23400(400)	3.75	0.089871619(1)	0.63 (2)	BCEP	
322418939	0.39	9.01	-2.65	0.65	26800(400)	4.44	0.161175643(2)	7.74 (2)	BCEP(C)	
330241794	0.27	9.96	-2.83	1.01	28800(300)	4.59	0.274758202(1)	4.69 (1)	BCEP(C)	
332158408	0.37	9.80	-2.42	1.33	24400(300)	4.35	0.244061039(3)	2.42 (1)	BCEP	
332499097	0.88	10.02	-1.76	1.23	18600(300)	3.19	0.187262382(2)	16.73(2)	BCEP?(C)	
339561272	0.64	10.01	-2.24	1.48	22700(500)	3.77	0.088337148(1)	1.35 (2)	BCEP(C)	
339570192	0.64	10.20	-2.28	1.32	23100(600)	3.64	0.094294761(1)	0.68 (1)	BCEP(C)	
341262179	0.62	9.26	-2.86	1.15	29200(200)	4.22	0.168535031(1)	20.58(1)	BCEP(C)	
344542087	0.33	10.70	-2.36	1.78	23800(500)	4.23	0.162795972(1)	2.82 (1)	BCEP	
372627092	0.34	10.70	-2.41	2.18	24300(400)	4.39	0.225308235(1)	11.40(1)	BCEP	
377768377	0.27	9.72	-2.16	0.57	21900(400)	4.22	0.180602029(1)	3.80 (1)	BCEP	
377895204	0.33	10.68	-2.54	2.14	25600(500)	4.45	0.118484236(1)	3.67 (1)	BCEP(C)	
381259601	0.38	9.65	-2.24	0.80	22600(400)	4.09	0.146601333(1)	1.87 (1)	BCEP	
383090276	0.25	11.32	-2.89	1.96	29500(700)	4.53	0.060149613(1)	2.09 (3)	BCEP(C)	
386693012	0.54	8.62	-2.46	0.53	24800(400)	4.18	0.073546294(1)	7.58 (1)	BCEP	(1)
391516015	0.40	9.62	-2.46	1.10	24800(500)	4.28	0.181821400(1)	4.14 (1)	BCEP(C)	
393346713	0.43	10.52	-2.52	1.66	25400(500)	4.10	0.112754739(1)	0.62 (1)	BCEP	
401122409	0.51	12.03	-1.79	2.03	18800(300)	3.21	0.092289677(1)	0.98 (3)	BCEP?	

(Continued)

Table 1. (Continued)

TESS ID	π (<i>mas</i>)	V (<i>Mag</i>)	<i>BC</i> (<i>Mag</i>)	<i>A_V</i> (<i>Mag</i>)	<i>T_{eff}</i> (<i>K</i>)	$\log(L/L_{\odot})$	Period (<i>days</i>)	Amplitude (<i>mmag</i>)	Comments	Flag
401975322	0.29	10.27	-2.61	0.42	26400(500)	4.07	0.107368784(1)	6.31 (1)	BCEP	
403378824	0.54	10.21	-2.16	1.20	21900(600)	3.69	0.105572076(1)	8.90 (1)	BCEP(C)	
409994572	1.10	7.99	-2.40	1.95	24200(400)	4.36	0.092277609(1)	1.50 (1)	BCEP	
422540366	0.26	11.11	-2.28	1.54	23000(400)	4.15	0.099244614(1)	1.09 (2)	BCEP(C)	
436285452	0.50	9.43	-2.28	0.85	23000(400)	3.97	0.105642375(1)	3.67 (1)	BCEP(C)	
437511417	0.54	9.28	-2.51	1.42	25300(400)	4.29	0.112221025(1)	1.99 (1)	BCEP	
438967685	0.71	9.88	-2.34	1.92	23600(400)	3.94	0.214345642(1)	3.40 (1)	BCEP(C)	
440132574	0.47	10.99	-2.75	2.60	27900(600)	4.30	0.090247548(1)	1.79 (1)	BCEP(C)	
440714949	0.47	10.32	-2.61	2.28	26300(700)	4.38	0.137889592(1)	12.22(1)	BCEP(C)	
441334176	0.47	9.92	-1.80	1.48	18900(300)	3.90	0.222130887(1)	0.19 (1)	BCEP?	
441675318	0.43	10.81	-2.86	1.55	29200(300)	4.07	0.126367362(1)	3.23 (1)	BCEP	
441875921	0.39	9.61	-2.65	0.70	26800(500)	4.20	0.084019404(1)	4.27 (1)	BCEP	
442942730	0.37	10.29	-2.76	1.82	28000(400)	4.49	0.139608794(1)	1.13 (1)	BCEP	
444357430	0.35	10.04	-2.55	1.75	25700(500)	4.52	0.262674343(1)	9.11 (1)	BCEP	
449614628	0.48	9.27	-2.43	0.81	24500(400)	4.12	0.072207624(1)	0.88 (1)	BCEP(C)	
450798851	0.65	9.48	-2.29	1.12	23200(400)	3.84	0.157869159(1)	3.35 (1)	BCEP(C)	
451123979	0.36	9.16	-2.67	0.66	27000(200)	4.46	0.068105858(1)	1.53 (1)	BCEP(C)	
451524691	0.37	10.20	-2.24	0.68	22600(300)	3.85	0.131394053(1)	2.25 (2)	BCEP(C)	
454954403	0.33	10.76	-2.69	2.01	27200(1000)	4.43	0.162146735(2)	21.64(2)	BCEP	
457764782	0.41	10.10	-2.52	1.07	25400(600)	4.07	0.172588294(1)	9.00 (1)	BCEP	
458235998	0.48	9.60	-2.12	0.42	21600(400)	3.71	0.156935036(1)	2.79 (1)	BCEP(C)	
458438308	0.40	10.57	-2.79	2.23	28300(500)	4.47	0.230050944(1)	56.49(5)	BCEP	
458561879	0.46	8.77	-2.15	0.51	21800(400)	4.12	0.158703061(1)	5.85 (1)	BCEP(C)	
458566069	0.40	9.72	-2.50	1.09	25200(500)	4.23	0.156554387(1)	5.46 (1)	BCEP(C)	
458833387	0.42	10.32	-2.46	1.89	24800(500)	4.25	0.207987915(1)	32.94(1)	BCEP	
459105076	0.97	9.59	-2.46	2.07	24800(300)	3.90	0.091531988(1)	2.34 (1)	BCEP(C)	(1)
459332381	0.44	9.78	-2.66	1.47	26800(400)	4.34	0.184129524(1)	7.97 (1)	BCEP(C)	
459675351	0.39	9.95	-2.85	1.10	29000(300)	4.31	0.146690576(1)	13.03(1)	BCEP(C)	
460412649	0.33	10.50	-2.19	0.77	22200(400)	3.85	0.190225162(1)	1.01 (1)	BCEP(C)	
460933755	0.11	11.49	-2.70	0.98	27300(1200)	4.69	0.093386494(1)	0.95 (2)	BCEP(C)	
462362757	0.38	11.19	-2.16	2.08	21900(500)	3.95	0.135783950(1)	4.61 (1)	BCEP	
462745510	0.41	9.90	-2.43	1.26	24400(500)	4.19	0.158740481(1)	5.96 (1)	BCEP	
463605260	0.49	10.26	-2.60	2.58	26200(800)	4.49	0.200982894(1)	1.13 (1)	BCEP	
464185342	0.47	9.36	-2.55	1.02	25700(400)	4.25	0.225357831(1)	5.73 (1)	BCEP(C)	
464188612	0.41	9.99	-2.14	1.09	21800(500)	3.97	0.129677312(1)	1.99 (1)	BCEP(C)	
464877141	0.33	10.85	-2.50	1.24	25200(600)	4.02	0.161205576(1)	16.50(2)	BCEP	
466592679	0.22	11.73	-2.41	1.52	24300(700)	4.10	0.180720462(1)	33.10(2)	BCEP(C)	
467279878	0.41	10.28	-2.33	1.56	23500(400)	4.11	0.150349062(2)	1.81 (2)	BCEP(C)	
467279937	0.44	10.22	-2.68	1.58	27100(700)	4.22	0.059846347(1)	1.01 (1)	BCEP(C)	
467547739	0.28	10.42	-2.25	0.77	22800(300)	4.03	0.174603422(1)	0.27 (1)	BCEP	
467880293	0.43	9.33	-2.29	0.66	23100(400)	4.07	0.181329693(1)	5.27 (1)	BCEP	
469395231	0.22	10.56	-2.63	1.37	26600(800)	4.58	0.118241552(1)	15.81(3)	BCEP(C)	
469533510	1.07	8.65	-2.28	1.45	23000(500)	3.87	0.061591120(1)	0.07 (1)	BCEP	

Note. Values in parentheses in Columns 6, 8, and 9 indicate the uncertainties. The capital letter "C" in Column 10 flags targets potentially affected by flux contamination from nearby sources within TESS apertures. Two objects

previously listed as candidate of BCEP stars by [Labadie-Bartz et al. \(2020\)](#) are annotated with "(1)" in Column 11.

ACKNOWLEDGMENTS

This work is partly supported by the International Cooperation Projects of the National Key R&D Program (No. 2022YFE0116800), the International Partnership Program of Chinese Academy of Sciences (No. 020GJHZ2023030GC), Chinese Natural Science Foundation (No. 12273103), Yunnan Revitalization Talent Support Program, and the basic research project of Yunnan Province (Grant Nos. 202501AS070055 and 202301AT070352). It is also funded by Chinese Academy of Sciences President's International Fellowship Initiative (Grant No. 2025PVA0089). This work has made use of data from the European Space Agency (ESA) mission Gaia (<https://www.cosmos.esa.int/gaia>), processed by the Gaia Data Processing and Analysis Consortium (DPAC, <https://www.cosmos.esa.int/web/gaia/dpac/consortium>). Funding for the DPAC has been provided by national institutions, in particular the institutions participating in the Gaia Multilateral Agreement. The TESS data presented in this paper were obtained from the Mikulski Archive for Space Telescopes (MAST) at the Space Telescope Science Institute (STScI). STScI is operated by the Association of Universities for Research in Astronomy, Inc. Support to MAST for these data is provided by the NASA Office of Space Science. Funding for the TESS mission is provided by the NASA Explorer Program. We are deeply appreciative of the insightful feedback provided by the anonymous referee, which has immensely improved the clarity and rigor of our paper.

REFERENCES

- Aerts, C., Christensen-Dalsgaard, J., & Kurtz, D. W. 2010, *Asteroseismology* (Dordrecht: Springer)
- Aerts, C., Thoul, A., Daszyńska, J., et al. 2003, *Science*, 300, 1926. doi:10.1126/science.1084993
- Aerts, C., Marchenko, S. V., Matthews, J. M., et al. 2006, *ApJ*, 642, 470. doi:10.1086/500800
- Balona, L. A. & Ozuyar, D. 2020, *MNRAS*, 493, 5871. doi:10.1093/mnras/staa670
- Baran, A. S. & Koen, C. 2021, *AcA*, 71, 113. doi:10.32023/0001-5237/71.2.3
- Briquet, M., Neiner, C., Aerts, C., et al. 2012, *MNRAS*, 427, 483. doi:10.1111/j.1365-2966.2012.21933.x
- Burssens, S., Bowman, D. M., Aerts, C., et al. 2019, *MNRAS*, 489, 1304. doi:10.1093/mnras/stz2165
- Burssens, S., Bowman, D. M., Michielsen, M., et al. 2023, *Nature Astronomy*, 7, 913. doi:10.1038/s41550-023-01978-y
- Dziembowski, W. A. & Pamiatnykh, A. A. 1993, *MNRAS*, 262, 204. doi:10.1093/mnras/262.1.204
- Dziembowski, W. A. & Pamiatnykh, A. A. 2008, *MNRAS*, 385, 2061. doi:10.1111/j.1365-2966.2008.12964.x
- Eze, C. I. & Handler, G. 2024, *ApJS*, 272, 2, 25. doi:10.3847/1538-4365/ad39c5
- Gaia Collaboration, Brown, A. G. A., Vallenari, A., et al. 2018, *A&A*, 616, A1
- Gaia Collaboration, Brown, A. G. A., Vallenari, A., et al. 2021, *A&A*, 649, A1. doi:10.1051/0004-6361/202039657
- Gaia Collaboration, Prusti, T., de Bruijne, J. H. J., et al. 2016, *A&A*, 595, A1. doi:10.1051/0004-6361/201629272
- Han, Z.-W., Ge, H.-W., Chen, X.-F., et al. 2020, *Research in Astronomy and Astrophysics*, 20, 161. doi:10.1088/1674-4527/20/10/161
- Handler, G., Jerzykiewicz, M., Rodríguez, E., et al. 2006, *MNRAS*, 365, 327. doi:10.1111/j.1365-2966.2005.09728.x
- Higgins, M. E. & Bell, K. J. 2023, *AJ*, 165, 4, 141. doi:10.3847/1538-3881/acb20c
- Jenkins, J. M., Caldwell, D. A., Chandrasekaran, H., et al. 2010, *ApJL*, 713, L87. doi:10.1088/2041-8205/713/2/L87
- Kurtz, D. W. 2006, *Communications in Asteroseismology*, 147, 6. doi:10.1553/cia147s6
- Labadie-Bartz, J., Handler, G., Pepper, J., et al. 2020, *AJ*, 160, 32. doi:10.3847/1538-3881/ab952c
- Langer, N., Schürmann, C., Stoll, K., et al. 2020, *A&A*, 638, A39. doi:10.1051/0004-6361/201937375
- Lenz, P. & Breger, M. 2005, *Communications in Asteroseismology*, 146, 53. doi:10.1553/cia146s53
- Mazumdar, A., Briquet, M., Desmet, M., et al. 2006, *A&A*, 459, 589. doi:10.1051/0004-6361:20064980
- Miglio, A., Montalbán, J., & Dupret, M.-A. 2007, *Communications in Asteroseismology*, 151, 48. doi:10.1553/cia151s48
- Montgomery, M. H. & Odonoghue, D. 1999, *Delta Scuti Star Newsletter*, vol. 13, p.28, 13
- Moskalik, P. & Dziembowski, W. A. 1992, *A&A*, 256, L5

- Murphy, S. J., Hey, D., Van Reeth, T., et al. 2019, *MNRAS*, 485, 2, 2380. doi:10.1093/mnras/stz590
- Paxton, B., Bildsten, L., Dotter, A., et al. 2011, *ApJS*, 192, 3. doi:10.1088/0067-0049/192/1/3
- Paxton, B., Cantiello, M., Arras, P., et al. 2013, *ApJS*, 208, 4. doi:10.1088/0067-0049/208/1/4
- Paxton, B., Marchant, P., Schwab, J., et al. 2015, *ApJS*, 220, 15. doi:10.1088/0067-0049/220/1/15
- Paxton, B., Schwab, J., Bauer, E. B., et al. 2018, *ApJS*, 234, 34. doi:10.3847/1538-4365/aaa5a8
- Paxton, B., Smolec, R., Schwab, J., et al. 2019, *ApJS*, 243, 10. doi:10.3847/1538-4365/ab2241
- Pedersen, M. G., Aerts, C., Pápics, P. I., et al. 2021, *Nature Astronomy*, 5, 715. doi:10.1038/s41550-021-01351-x
- Pedersen, M. G., Escorza, A., Pápics, P. I., et al. 2020, *MNRAS*, 495, 2738. doi:10.1093/mnras/staa1292
- Pigulski, A. & Pojmański, G. 2008, *A&A*, 477, 917. doi:10.1051/0004-6361:20078581
- Ramspeck, M., Heber, U., & Moehler, S. 2001, *A&A*, 378, 907. doi:10.1051/0004-6361:20011246
- Ricker, G. R., Winn, J. N., Vanderspek, R., et al. 2015, *Journal of Astronomical Telescopes, Instruments, and Systems*, 1, 014003. doi:10.1117/1.JATIS.1.1.014003
- Sadowski, A., Belczynski, K., Bulik, T., et al. 2008, *ApJ*, 676, 1162. doi:10.1086/528932
- Shi, X.-D., Qian, S.-B., Li, L.-J., et al. 2021, *AJ*, 161, 46. doi:10.3847/1538-3881/abccd7
- Shi, X.-D., Qian, S.-B., Li, L.-J., et al. 2021, *MNRAS*, 505, 6166. doi:10.1093/mnras/stab1657
- Shi, X.-D., Qian, S.-B., Li, L.-J., et al. 2021, *PASP*, 133, 054201. doi:10.1088/1538-3873/abf32a
- Shi, X.-D., Qian, S.-B., & Li, L.-J. 2022, *ApJS*, 259, 50. doi:10.3847/1538-4365/ac59b9
- Shi, X.-D., Qian, S.-B., Zhu, L.-Y., et al. 2023, *ApJS*, 265, 33. doi:10.3847/1538-4365/acba91
- Shi, X.-D., Qian, S.-B., Zhu, L.-Y., et al. 2023, *ApJS*, 268, 16. doi:10.3847/1538-4365/ace88c
- Shi, X.-D., Qian, S.-B., Zhu, L.-Y., et al. 2024, *ApJS*, 271, 1, 28. doi:10.3847/1538-4365/ad1f66
- Stankov, A. & Handler, G. 2005, *ApJS*, 158, 193. doi:10.1086/429408
- Stassun, K. G., Oelkers, R. J., Pepper, J., et al. 2018, *AJ*, 156, 102. doi:10.3847/1538-3881/aad050
- Vink, J. S., de Koter, A., & Lamers, H. J. G. L. M. 2001, *A&A*, 369, 574. doi:10.1051/0004-6361:20010127
- Wenger, M., Ochsenbein, F., Egret, D., et al. 2000, *A&AS*, 143, 9. doi:10.1051/aas:2000332
- Yoon, S.-C., Woosley, S. E., & Langer, N. 2010, *ApJ*, 725, 940. doi:10.1088/0004-637X/725/1/940